Supplementary conceptual model:

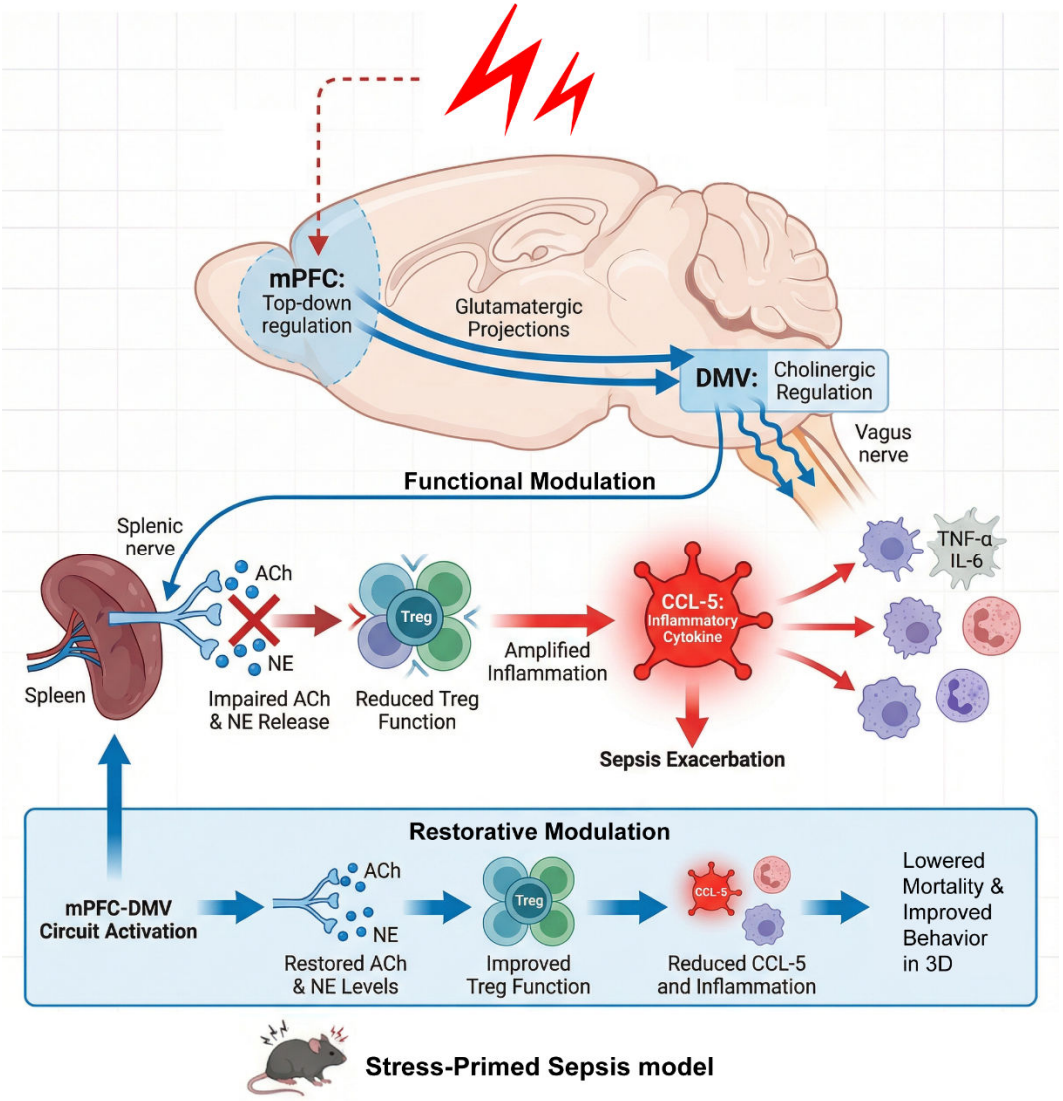

Schematic summary of the revised functional framework illustrating how stress-induced cortical dysfunction alters central autonomic modulation and downstream immune outcomes in sepsis.

Supplementary Methods

This appendix provides detailed experimental procedures corresponding to the Methods section in the main manuscript.

Animals

Adult male ChAT-Cre transgenic mice (6–8 weeks old) were purchased from Jackson Laboratory (Bar Harbor, ME, USA), and C57BL/6J mice were obtained from Charles River Co., Ltd. (Beijing, China). Only male mice were used to eliminate variability related to the estrous cycles. The animals were randomly assigned to the experimental

groups using a random number generator. The sample size was determined based on a previous study [1]. Mice showing no detectable fluorescence after viral transfection or unsuccessful injections were excluded from the analysis. Animal experiments were performed according to the procedures approved by the Animal Care and Use Committee of the Fourth Military Medical University (Xi'an, China; study number KY20233257-1; approved May 3, 2023) and conducted in accordance with the institutional Guidelines for Animal Experimentation and the Animal Research: Reporting of In Vivo Experiments (ARRIVE) guidelines.

Statistical Analysis

For time-course analyses (e.g., body weight and serum cytokine levels), data were analyzed using two-way repeated-measures ANOVA with group and time as factors, followed by Bonferroni-corrected post hoc comparisons when significant main effects or interactions were detected. Detailed procedures for c-Fos immunohistochemistry and quantification are provided in the SI Appendix.

Stereotaxic Surgery and Viral Delivery

The mice were anesthetized with pentobarbital sodium (100 mg kg^{-1}, intraperitoneally) and positioned in a stereotaxic frame for the experiment. The scalp was shaved, and the skin was locally anesthetized with 2.0% lidocaine. A midline sagittal incision was made, and small craniotomies were drilled at the following coordinates relative to the bregma: for the dorsal motor nucleus of the vagus (DMV), anteroposterior (AP) −6.75 mm, mediolateral (ML) ±0.65 mm, and dorsoventral (DV) −3.6 mm; and for the medial prefrontal cortex (mPFC), AP +1.9 mm, ML ±0.3 mm, and DV −1.4 mm. Viral solutions were delivered at a rate of 50 nl min^{-1} (200 nl per side) using a glass micropipette connected to a micro-syringe pump. The pipette was left in place for 10 min before a slow withdrawal to minimize backflow. Postsurgical care included placement on a warming pad until full recovery from anesthesia and administration of meloxicam (0.03 mg kg^{-1}, subcutaneously) for three days after the surgery. All in vivo electrophysiological, splenic nerve activity, and behavioral experiments were conducted at least three weeks after surgery to ensure recovery and robust viral expression. For all in vivo circuit-manipulation experiments involving

DREADDs, control groups received clozapine-N-oxide (CNO i.p.,5mg/kg) administration following injection of control AAV-DIO-mCherry viruses (CNO-only controls). Detailed information on all viral vectors used for chemogenetic manipulation and circuit tracing is provided in the SI Appendix.

Ex vivo Patch-Clamp Electrophysiology

The incubated brain slices were transferred to a recording chamber and continuously superfused with oxygenated artificial cerebrospinal fluid (aCSF) for the duration of the experiment. The dorsal motor nuclei of the vagus (DMV) and medial prefrontal cortex (mPFC) regions were identified in each slice according to the mouse brain atlas, and DMV^{ChAT} or $mPFC^{Glut}$ neurons were visualized under a DM LFSA microscope (Leica, Wetzlar, Germany). Recording electrodes (3–6 MΩ) were filled with an intracellular solution. Signals were amplified using a Multiclamp 700B patch-clamp amplifier, digitized using a Digidata 1550B interface, and acquired using the Clampex 10.5 software (Molecular Devices). The data were sampled at 10 kHz and low-pass filtered at 2 kHz, respectively. All recordings were conducted at room temperature (25–30 ℃).

Spontaneous Excitatory Postsynaptic Currents (sEPSCs)

For sEPSC recordings, picrotoxin (PTX; 100 μM) was added to the perfusate to block GABAA receptor-mediated currents. The pipette solution contained (in mM) 120 potassium gluconate, 20 KCl, 2 $MgCl_2$, 0.2 EGTA, 10 HEPES, 4 Na_2-ATP, and 0.3 GTP (pH 7.3, adjusted with KOH). Neurons were voltage-clamped at −60 mV in gap-free mode, and sEPSCs were recorded for 10 min per cell. For the analysis, a stable 3-min segment was selected, and the event amplitudes and frequencies were quantified.

Intrinsic Excitability

Intrinsic excitability was assessed in the presence of PTX (100 μM), CNQX (20 μM), and AP-V (50 μM) to block the synaptic transmission. Using the same intracellular solution, a whole-cell configuration was established, and the neurons were allowed to stabilize in the I = 0 mode. If necessary, a holding current of < 50 pA was applied to adjust the membrane potential to the resting level. For DMV^{ChAT} neurons, step

currents from 0 to 150 pA (10 pA increments, 500 ms duration, 15 s intersweep interval) were injected into the cells. For $mPFC^{Glut}$ neurons, step currents from 0 to 300 pA (50 pA increments, 2000 ms duration, and 15 s intersweep interval) were applied. Before each depolarizing step, a hyperpolarizing pulse (−40 pA, 400 ms) was delivered to measure the voltage responses, and the input resistance was calculated using Ohm's law. Cells with >20% change in input resistance during recording were excluded from the analysis.

For electrophysiological recordings, individual cells were treated as independent observations, with 2–3 cells recorded per animal; animals were sampled across experimental groups.

Splenic Nerve Activity Recording and Circuit Intervention

The mice were anesthetized with isoflurane and implanted with wireless neural recording electrodes, according to the manufacturer's instructions (Shanghai QuanLan Technology Co., Ltd.). After the fur was shaved, the head-mounted connector of the wireless signal acquisition device was fixed to the skull using stainless-steel screws and dental cement. A cuff electrode preconnected to the recording interface was tunneled subcutaneously from the skull to the abdominal region through the cervical route.

Following skin preparation and disinfection of the abdominal area, a small midline laparotomy was performed to gently expose the splenic hilum for cannulation of the splenic veins. The splenic nerve was bluntly dissected from the surrounding tissue, and a cuff electrode was placed longitudinally along the nerve's surface. The spleen was carefully returned to its anatomical position, and the abdominal musculature and skin were sutured in the layers. The second disinfection was performed before the recovery process.

Postoperative care included placement on a warming pad until full recovery from anesthesia and administration of meloxicam (0.03 mg kg^{-1}, subcutaneously) once daily for three days after surgery. Circuit manipulations were conducted after full recovery and paired with simultaneous splenic nerve activity recordings to assess the effects of DMV or mPFC-DMV intervention.

Recording Data Analysis

The splenic nerve activity signals were sampled at 500 Hz. The raw recordings were digitally bandpass-filtered between 10 and 60 Hz to minimize the baseline drift and high-frequency noise. Spike events were detected in MATLAB (R2024b, MathWorks) using the findpeaks function, with the amplitude threshold set to the mean ± 1 standard deviation of the signal amplitude at each recording point. The mean spike count per 1-s bin was calculated over a continuous 3,600-s recording period for each mouse in its home cage. Group differences in mean firing rates were analyzed using one-way ANOVA, followed by appropriate post hoc multiple comparison tests.

Flow Cytometry

Splenocyte Isolation

Spleens were harvested from the mice immediately after euthanasia and placed in ice-cold sterile PBS. Each spleen was gently dissociated using a sterile syringe plunger until no visible red tissue fragments were present. The cell suspension was passed through a 70-μm nylon mesh filter and rinsed with 2% RPMI-1640 medium. The filtrate was collected in 15-mL conical tubes and centrifuged at 1,600 rpm for 5 min at 4 ℃. The supernatant was discarded, and the cell pellet was resuspended in 10 mL PBS and centrifuged under the same conditions. Red blood cells were lysed by resuspending the pellet in 2–3 mL of 1× RBC lysis buffer and incubating on ice for 5–10 min. Lysis was stopped by adding 10 mL of PBS, and the cells were centrifuged. The pellet was finally resuspended in 2% RPMI-1640 medium. Large tissue clumps were removed, and the viable cells were counted.

Cell Surface Staining

Splenocytes were transferred into 1.5-mL tubes, centrifuged at 1,600 rpm for 5 min, and washed once with 500 μL of PBS. The cell pellet was resuspended in 50 μL of pre-prepared antibody staining buffer for surface markers (antibody panels prepared according to the manufacturer's instructions) and incubated at room temperature for

30 min in the dark. After incubation, the cells were washed with 500 μL PBS and centrifuged at 1,600 rpm for 5 min.

Fixation, Permeabilization, and Intracellular Staining

Cells were fixed in 250 μL of fixation buffer for 20 min at room temperature in the dark, followed by incubation with 250 μL of 1× permeabilization buffer for 10 min. After permeabilization, the cells were centrifuged (2,200 rpm, 5 min), the supernatant was discarded, and 500 μL of 1× permeabilization buffer was added for a single wash. The cell pellet was then resuspended in 50 μL of pre-prepared intracellular antibody staining solution and incubated for 30–40 min at room temperature in the dark, according to the manufacturer's instructions. Following incubation, the cells were washed twice with 500 μL PBS (2,200 rpm, 5 min each) and resuspended in 200–300 μL PBS for flow cytometric acquisition. If immediate analysis was not performed, the samples were stored at 4 ℃ in the dark until further processing.

Neurotransmitter Extraction and LC–MS/MS Analysis

Following euthanasia, splenorenal tissue was rapidly isolated on ice and immediately snap-frozen at −80 ℃, as described previously [2]. Benzoyl chloride derivatization was performed before the analysis. Neurotransmitter quantification was performed using an ACQUITY Premier UPLC system (Waters) equipped with an ACQUITY UPLC HSS T3 column (100 × 2.1 mm, 1.8 μm). Multiple reaction monitoring (MRM) data were acquired and processed using SCIEX Analyst Work Station Software (version 1.6.3) and Biobud-DDF (version 2.0.3.11).

Metabolomic Data Acquisition and Analysis

Following sample pretreatment, metabolite profiling was performed using an AB SCIEX 5500 QQQ-MS mass spectrometer, and biochemical analyses were performed. Quality control (QC) samples were included to assess data stability, as recommended for mass-spectrometry-based metabolomics. Although QC samples are theoretically identical, systematic errors during sample extraction, detection, and analysis can introduce variations. The data quality was evaluated by calculating the relative

standard deviation (RSD) of each targeted metabolite within the QC samples, with an RSD of < 10% indicating high-quality data.

For statistical analysis, Student's *t-test* was applied to identify metabolites showing significant differences between the comparison groups, with $p < 0.05$ considered to indicate statistical significance. The abundances of differentially abundant metabolites were normalized using the *z-score* method and visualized via hierarchical clustering in R (pheatmap package) to illustrate the differences in accumulation between groups.

3D-AI Animal Behavior Analysis System

3D Behavioral Analysis

A multimodal behavioral analysis pipeline was established to convert 2D video recordings into 3D behavioral representations, as previously described[3]. During testing, a synchronized multicamera video acquisition system (resolution 960 × 540, frame rate 30 fps) was positioned around a circular open-field arena (diameter: 40 cm). The inner wall of the arena was thoroughly cleaned with 75% ethanol before each trial to eliminate any residual odors. Each mouse was recorded for 10 min of continuous, free exploration. From each recording, 800 frames were extracted for the manual annotation of 16 anatomical landmarks (nose, left ear, right ear, neck, left forelimb, right forelimb, left hind limb, right hind limb, left forepaw, right forepaw, left hind paw, right hind paw, back, tail base, tail middle, and tail tip). The annotations were verified in a double-blind manner to ensure accuracy.

The annotated dataset was used for transfer learning of a deep convolutional neural network with spatiotemporal feature extraction capability to enable automated pose estimation across all the video frames. Keypoint positions from four synchronized 2D projections were geometrically corrected and reconstructed into a 3D skeletal model using multi-view triangulation. For the reconstructed spatiotemporal sequences, hierarchical clustering analysis was applied to segment the behavior into 40 distinct action units with precise timestamps.

The resulting multidimensional behavioral representation matrix integrates millisecond-level temporal features, 3D kinematic parameters (joint angle and limb

length variation rates), and action classification labels. Nonlinear dimensionality reduction was performed using the uniform manifold approximation and projection (UMAP) algorithm for behavioral state visualization.

To assign an ethical meaning, each of the 40 behavior units was manually labeled according to the Mouse Ethogram database and the literature, yielding a standardized set of named behavioral subtypes for subsequent statistical analyses.

Viral vectors and chemogenetic tools

The following viral vectors were used in this study. For chemogenetic manipulation of cholinergic neurons, AAV2/9-ChAT-DIO-hM3Dq-mCherry and AAV2/9-ChAT-DIO-hM4Di-mCherry (BrainVTA, Wuhan, China) were used. For projection-defined circuit targeting, AAV2/1-hSyn-Cre (BrainVTA) and AAV2/Retro-CaMKIIα-Cre (BrainVTA) were employed as indicated.

For retrograde and transsynaptic tracing, PRV-EGFP (200 nL per injection; BrainVTA) was used for splenic nerve–associated tracing. Monosynaptic rabies-based tracing was performed using a combination of AAV vectors encoding TVA and rabies glycoprotein (RG) together with RVΔG-EGFP, as described in the experimental procedures. All rabies-related viral components were obtained from BrainVTA. All viral aliquots were stored at −80 °C and thawed immediately prior to use. Injection volumes and stereotaxic coordinates for each experiment are described in the corresponding sections below.

c-Fos immunohistochemistry and quantification

Neuronal activity–associated signaling was assessed using c-Fos immunohistochemistry. Twenty-four hours after experimental initiation, mice were deeply anesthetized and transcardially perfused with phosphate-buffered saline followed by 4% paraformaldehyde. Brains were removed, post-fixed overnight, cryoprotected in 30% sucrose, and sectioned coronally at 30 μm thickness using a cryostat.

Free-floating sections containing the medial prefrontal cortex (mPFC) or dorsal motor nucleus of the vagus (DMV) were processed for immunostaining. Sections were

blocked and incubated with a rabbit anti-c-Fos primary antibody (1:500; Sigma-Aldrich), followed by species-appropriate fluorescent secondary antibodies. All staining procedures were performed in parallel across experimental groups to minimize batch effects.

For each animal, three anatomically matched sections per region were selected for analysis. c-Fos–positive cells were quantified using ImageJ/FIJI software with consistent thresholding parameters applied across all images. Cell counting was performed by an experimenter blinded to experimental group assignment. c-Fos expression was interpreted as a surrogate marker of neuronal activity–associated signaling rather than a direct measure of neuronal firing.

Supplementary Figures:

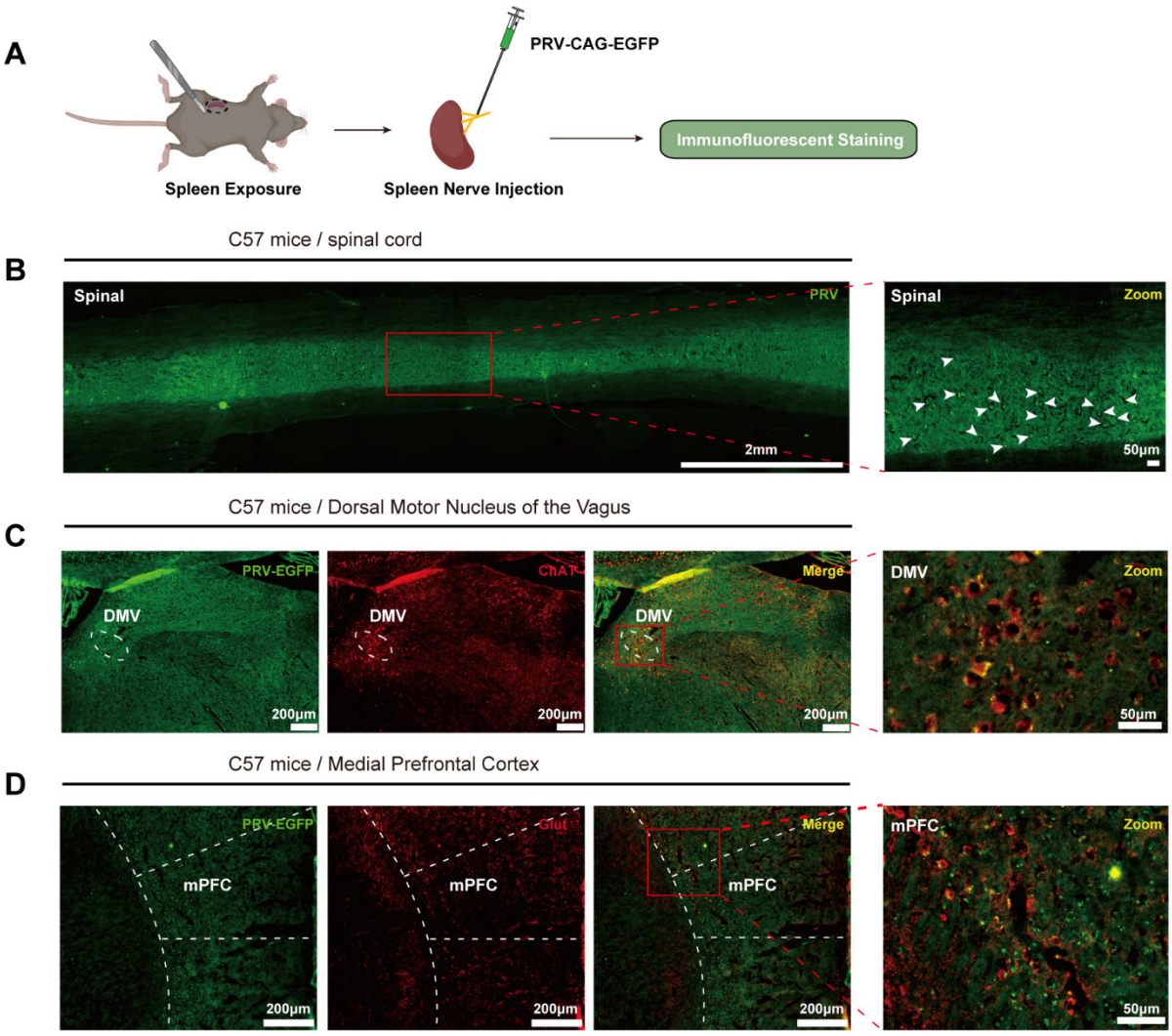

Fig. S1. Central DMV cholinergic and mPFC glutamatergic neurons are linked to splenic regulation through autonomic pathways.

(A) Experimental timeline and schematic representation of this study.

(B) Left: Expression of green fluorescent protein-labeled polysynaptic retrograde tracer PRV-EGFP in the spinal cord following injection into the splenic nerve; right: enlarged view of the indicated region and the white arrow indicate the infected neurons.

(C) PRV-EGFP labeling in the dorsal motor nucleus of the vagus (DMV) showing colocalization with cholinergic neurons (ChAT$^+$, red); right: magnified regional view of the DMV.

(D) PRV-EGFP labeling in the medial prefrontal cortex (mPFC) with colocalization to Glutamatergic neurons (red); right panel shows a magnified regional view.

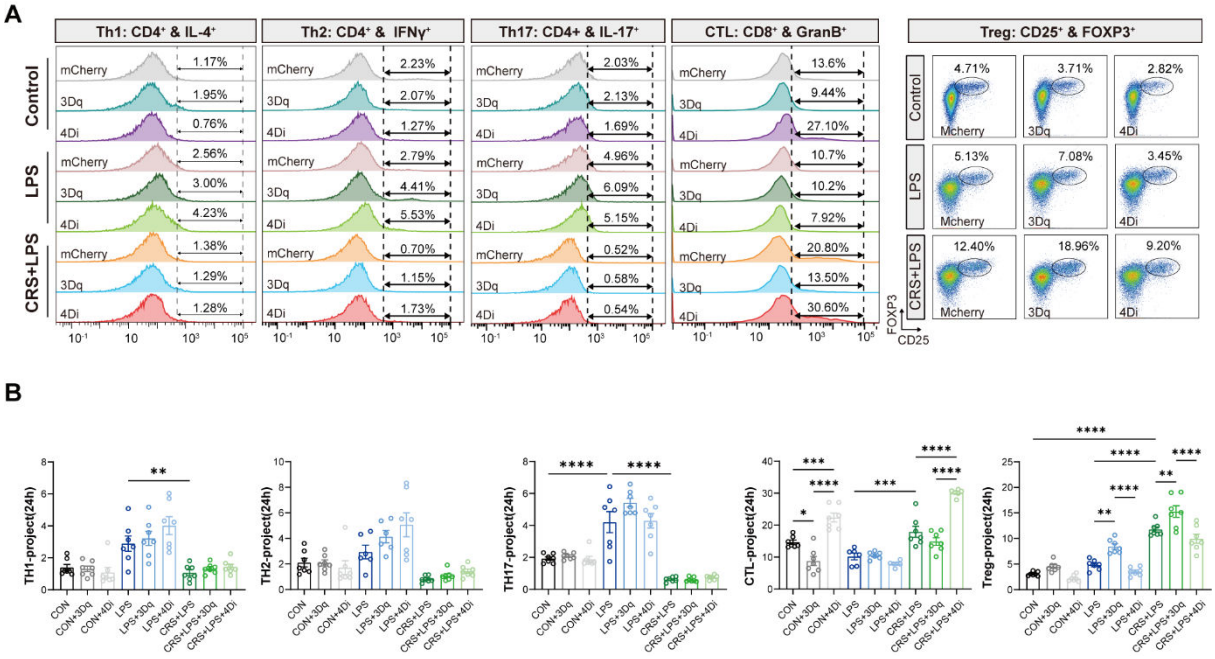

Fig. S2. Activation of mPFC–DMV glutamatergic projections selectively rescue Treg deficits in stress-primed sepsis.

(A) Representative flow cytometry plots showing Th1, Th2, Th17, CTLs, and Tregs in the control, LPS, and CRS + LPS groups and in each group following bidirectional chemogenetic modulation of mPFC glutamatergic projections to the DMV.

(B) Quantification of splenic T-cell subset frequencies (Th1, Th2, Th17, CTLs, and Tregs) in the experimental group. Data are presented as the mean ± SEM and were

analyzed using one-way ANOVA with Bonferroni post hoc correction for multiple comparisons.

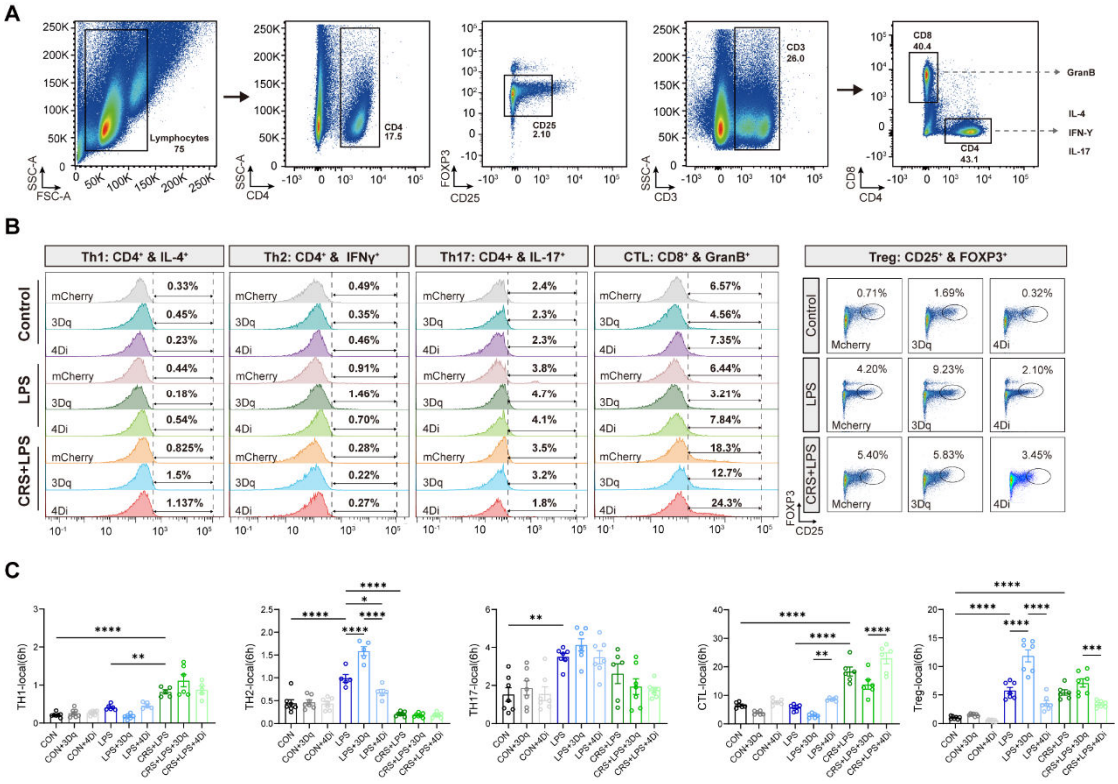

Fig. S3. Early activation of DMV cholinergic neurons fails to alter all splenic T-cell responses during the acute phase of stress-primed sepsis.

(A) Schematic representation of immune cell classification and gating markers used in flow cytometry.

(B) Representative flow cytometry plots showing the activity of Th1 cells, Th2 cells, Th17 cells, CTLs, and Tregs in the control, LPS, and CRS + LPS groups and in each group after bidirectional chemogenetic modulation of the DMV cholinergic neurons.

(C) Quantification of splenic T-cell subset frequencies (Th1, Th2, Th17, CTLs, and Tregs) in the experimental groups. Data are presented as the mean ± SEM and were analyzed using one-way ANOVA with Bonferroni post hoc correction for multiple comparisons.

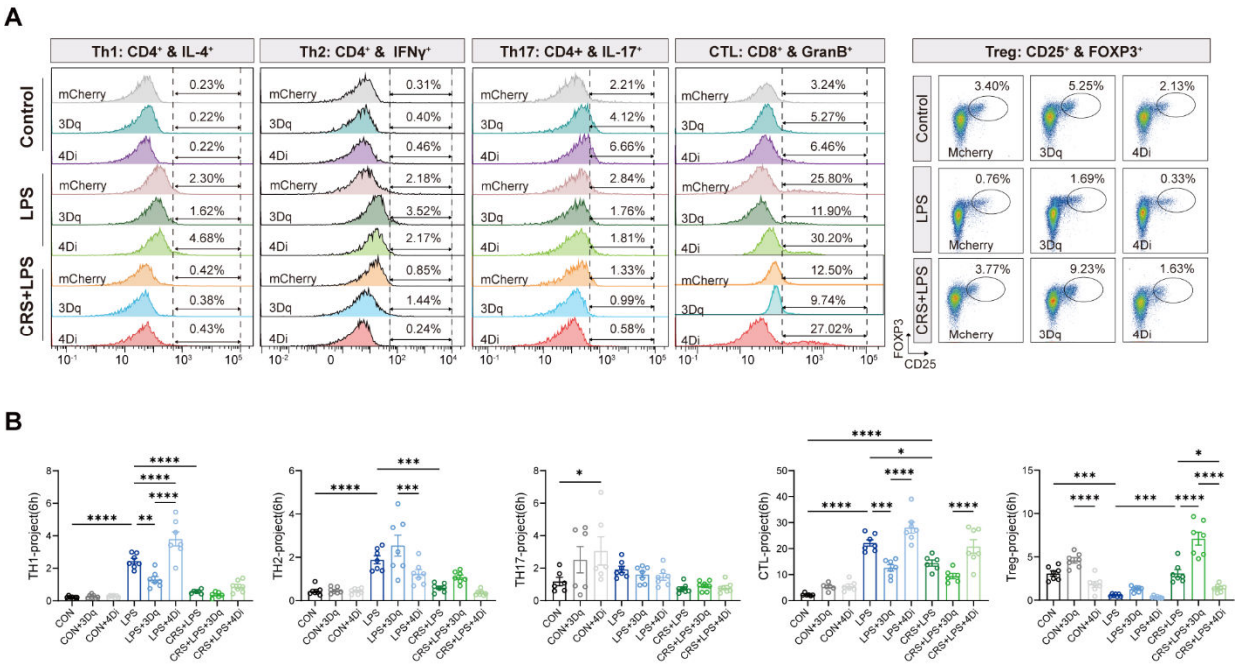

Fig. S4. mPFC–DMV circuit modulation does not affect all splenic T-cell activity during the early phase of stress-primed sepsis.

(A) Representative flow cytometry plots showing the activity of Th1, Th2, Th17, CTLs, and Tregs in the control, LPS, and CRS + LPS groups and in each group after bidirectional chemogenetic modulation of mPFC glutamatergic projections to the DMV.

(B) Quantification of splenic T-cell subset frequencies (Th1, Th2, Th17, CTLs, and Tregs) in the experimental groups. Data are presented as the mean ± SEM and were analyzed using one-way ANOVA with Bonferroni post hoc correction for multiple comparisons.

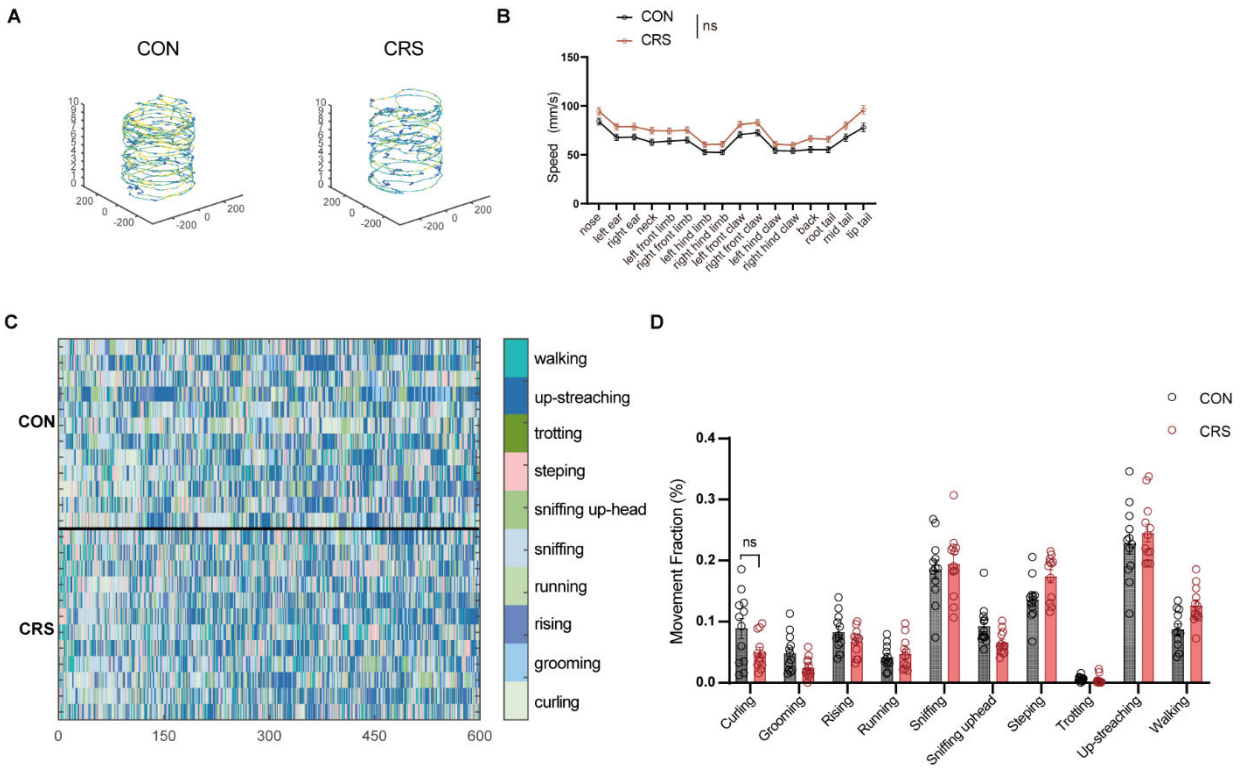

Fig. S5. Chronic stress alone does not alter baseline locomotor or behavioral states.

(A) Representative movement trajectories of the CON and CRS groups.

(B) Statistical comparison of body anchor points velocities across the groups.

(C) Behavioral ethogram heatmaps showing the temporal distribution of the identified modes across the recording period.

(D) Quantification of the relative proportions of the ten behavioral modes in each group. Data are presented as the mean ± SEM; * $P < 0.05$, ** $P < 0.01$ (one-way ANOVA with Tukey's test).

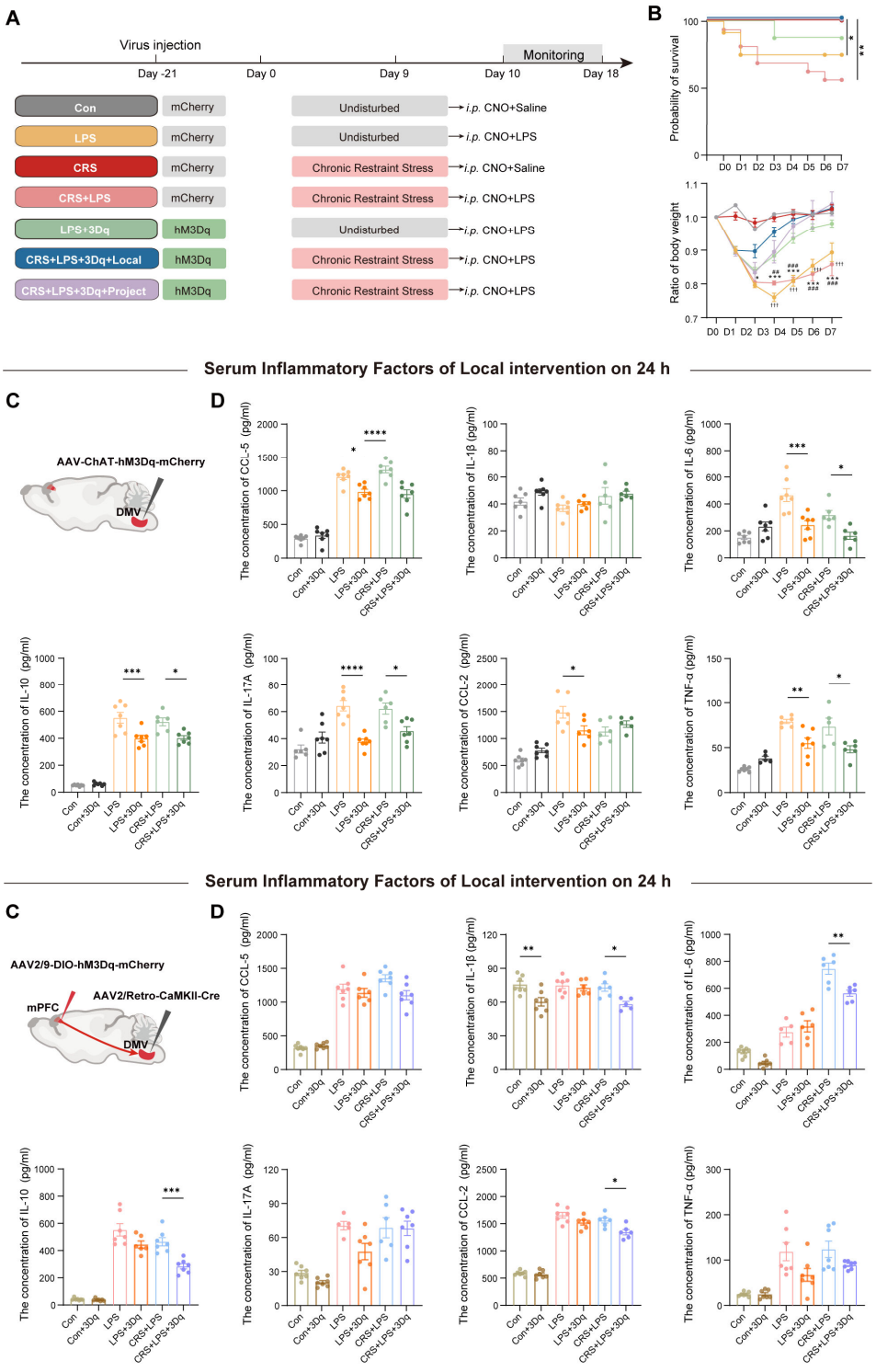

Fig. S6. Reactivation of the mPFC–DMV pathway reduces systemic inflammation, improves recovery, and lowers mortality in stress-primed sepsis.

(A) Experimental timeline and schematic representation of this study.

(B) Kaplan–Meier survival curves depicting the specific survival rates in the LPS, CRS, CRS + LPS, LPS+3Dq, CRS + LPS+3Dq (projection) and CRS + LPS+3Dq (local) groups (upper). And Seven-day profile of body weight changes in the CON,

LPS, CRS, CRS + LPS, LPS+3Dq, CRS + LPS+3Dq (projection), and CRS + LPS+3Dq (local) groups (bottom)(Two-way ANOVA: *** $p < 0.001$ for CRS + LPS vs. CRS + LPS+3Dq+Local; $^{###}$ $p < 0.001$ for CRS + LPS vs. CRS + LPS+3Dq+Project; ††† $p < 0.001$ for LPS vs. LPS+3Dq+Local).

(Ci) Schematic representation of the viral injection sites and local DMV^{ChAT} modulation.

(Di) Quantification of serum levels of the inflammatory factors IL-1β, IL-6, IL-10, IL-17A, CCL-2, CCL-5 and TNF-α following chemogenetic activation of DMV^{ChAT} neurons 24 h after sepsis induction.

(Cii) Schematic representation of the viral injection sites and projection modulation from $mPFC^{glu}$ to DMV.

(Dii) Quantification of serum levels of the inflammatory factors IL-1β, IL-6, IL-10, IL-17A, CCL-2, CCL-5 and TNF-α following chemogenetic activation of $mPFC^{glu}$-DMV circuit 24 h after sepsis induction.

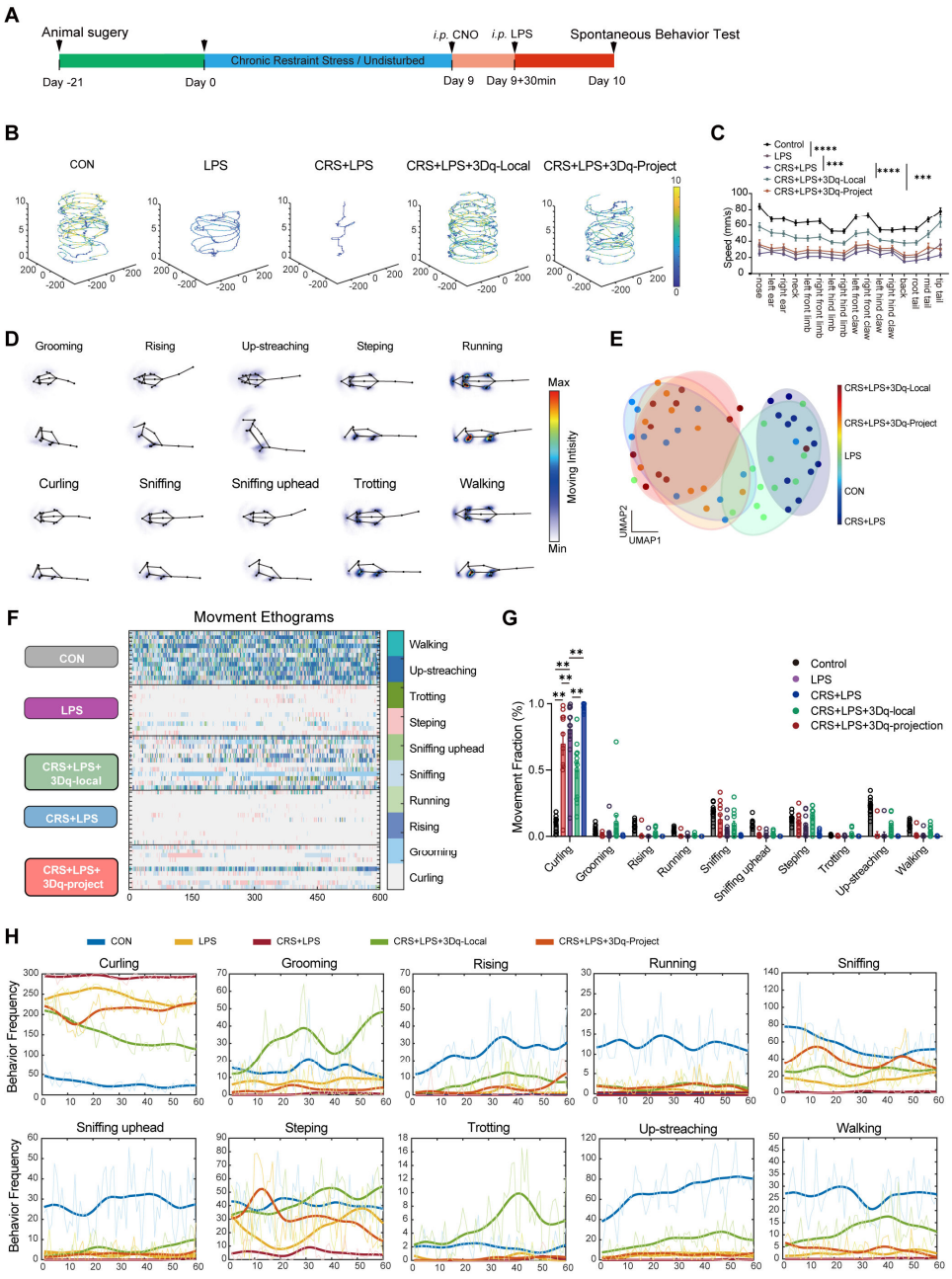

Fig. S7. mPFC–DMV circuit activation restores sepsis-altered behavioral states and improves functional outcomes after stress priming.

(A) Experimental workflow and schematic of behavioral tracking.

(B) Representative movement trajectories of each group.

(C) Statistical comparison of body anchor point velocities across the groups.

(D) Nomenclature and skeletal representations of the ten identified behavioral modes.

(E) UMAP dimensionality reduction plots for the control, LPS, CRS + LPS, CRS + LPS + DMV cholinergic neuron activation, and CRS + LPS + mPFC glutamatergic projection-to-DMV activation groups.

(F) Behavioral ethogram heatmaps showing the temporal distribution of the identified modes across the recording period.

(G) Quantification of the relative proportions of the ten behavioral modes in each group.

(**H**) Faction of five behavioral categories. Data are presented as the mean ± SEM; **P* < 0.05, ** *P* < 0.01 vs. control (two-way ANOVA with Tukey's test).

Referance:

1. Zhai Q, Lai D, Cui P, et al. Selective Activation of Basal Forebrain Cholinergic Neurons Attenuates Polymicrobial Sepsis-Induced Inflammation via the Cholinergic Anti-Inflammatory Pathway. *Crit Care Med* 2017; **45**(10): e1075–e82.
2. Wang Y, Zhang Y, Wang K, et al. Esketamine increases neurotransmitter releases but simplifies neurotransmitter networks in mouse prefrontal cortex. *J Neurophysiol* 2022; **127**(2): 586–95.
3. Huang K, Han Y, Chen K, et al. A hierarchical 3D-motion learning framework for animal spontaneous behavior mapping. *Nat Commun* 2021; **12**(1): 2784.